# Dictating $CO_2$ Reduction Selectivity through Electrocatalyst Microenvironment Modification: The Effect of Catholyte and Catalyst Layer Binder Composition

Yingying Chen [a,1], Jacob A. Wrubel[a,1], Ashlee E. Vise[a], Fry Intia[a], Samantha Harshberger[b], Ellis Klein[a], Wilson A. Smith[a,c,d], Zhiwen Ma[a], Todd G. Deutsch[a], and Kenneth C. Neyerlin[a,*]

[1]These authors contributed equally to this work and are listed alphabetically.

[a] National Renewable Energy Laboratory, Golden, CO 80401

[b] Front Range Community College, Westminster, CO 80031

[c] Department of Chemical and Biological Engineering, University of Colorado Boulder, Boulder, CO 80303

[d] Renewable and Sustainable Energy Institute (RASEI), University of Colorado Boulder, Boulder, CO 80303

*Corresponding Author: Kenneth.Neyerlin@nrel.gov*

**Abstract**

Electrochemical reduction of carbon dioxide ($CO_2$) is an attractive technology to convert waste $CO_2$ to value-added chemicals using renewably generated electricity. In this work, we combine both experimental and theoretical analyses to investigate the factors affecting the Faradaic efficiency (FE) of the $CO_2$ electrolysis cell, including different catalysts (Ag/Vu and $SnO_2$/Vu, where Vu is Vulcan carbon black), binder materials and catholyte compositions. The FE of the cell was measured experimentally across various electrode compositions and system conditions to understand their impact on the branching ratios of the two-electron $CO_2$ reduction products – CO and formate. As a complementary effort, a 2D multiphysics transport model was developed and used to elucidate the fundamental process occurring in the cathode electrode. The ionic concentrations throughout the electrode and the catholyte layer were also determined. It was shown that the selectivity of $CO_2$ reduction to CO can change significantly when different catholyte compositions and binder materials are used. In contrast, the selectivity of $CO_2$ to formate is relatively stable across the range of conditions studied. These insights can be used to inform decisions regarding the electrode development and system design in $CO_2$ electrolyzers and ultimately contribute to scaling energy efficient electrochemical $CO_2$ reduction systems.

*Graphical Abstract:*

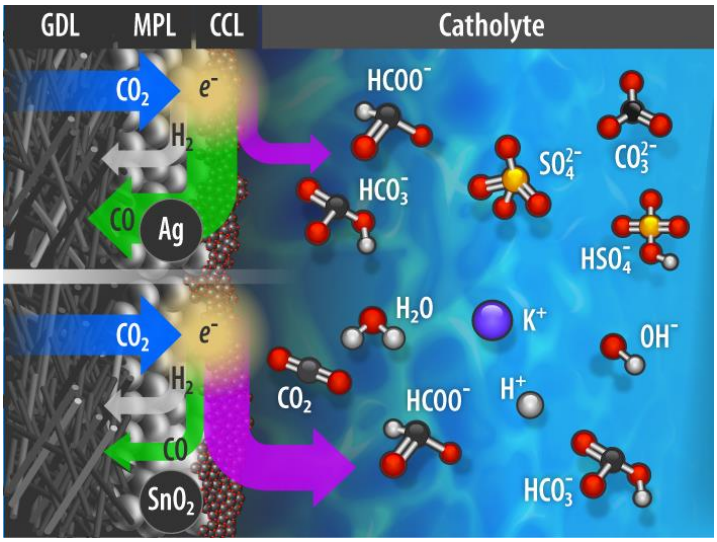

## 1. Introduction

Electrochemical reduction of carbon dioxide ($CO_2$) is an attractive technology for energy conversion and storage. The penetration of renewable energy sources like wind and solar continues to increase, but these technologies are variable both daily and seasonally, meaning they may not be able to produce dispatchable power on demand. This variability presents a challenge for reliable grid-scale integration of these technologies. Electrons to molecules techniques, which use electricity to generate storable and energy-dense fuels, can leverage the clean and abundant electrons from renewables and offset their intermittency issues. Electrochemical $CO_2$ reduction ($CO_2R$) is one such electrons to molecules pathway that has the added benefit of utilizing the most significant greenhouse gas in terms of radiative forcing and reducing anthropogenic $CO_2$.[1] In addition, techno-economic analysis has shown that the price of electricity is the most significant driver of the levelized cost of $CO_2R$ products,[2,3] meaning that there exists a promising symbiosis between renewables and electrochemical $CO_2R$.[4] However, electrochemical $CO_2R$ is still a relatively new technology and there are many fundamental questions that must be addressed before it can be considered a viable industrial process.[4–6]

Low temperature electrochemical $CO_2R$ cells can use $CO_2$ in either liquid or gaseous form. Liquid-fed cells use a catholyte containing $HCO_3^-$ or $CO_3^{2-}$ ions or dissolved $CO_2$,[7,8] while gas-fed cells use a gas diffusion layer (GDL) to transport gaseous $CO_2$ to the electrochemical reaction sites.[6,9–11] This work employs a gas-fed cell with a gas diffusion electrode (GDE) as the cathode, shown schematically in Figure 1a. A catholyte layer was introduced between the bipolar membrane (BPM) and the cathode to improve the selectivity of $CO_2R$ products.[12] Under certain voltages, the oxygen evolution reaction (OER) occurs at the anode, while $CO_2R$ and the competitive hydrogen evolution reaction (HER) occur in parallel at the cathode. $CO_2R$ can result in dozens of different products depending on the electrocatalyst, cell configuration, and other material properties, which leads to highly coupled reaction schemes.[13,14] In this work, Ag/Vu and $SnO_2$/Vu (where Vu refers to Vulcan carbon black) were used as the catalyst in the cathode GDE; for these materials the major $CO_2R$ products are carbon monoxide ($CO$) and formate ($HCOO^-$).

$CO$ and formate are among the easiest targets for electrochemical $CO_2R$ because they involve the addition of only two electrons. This means that their respective reaction mechanisms are simpler than further reduced products like methanol ($CH_3OH$, six electrons) and methane ($CH_4$, eight electrons).[15] Formic acid is useful in industrial and agricultural industries[16–19], while CO can

be a useful precursor to other hydrocarbon fuels.[20] While these products can be produced at some of the highest Faradaic efficiencies (FEs) reported in the literature, their reaction mechanisms and the factors affecting the reaction efficiencies at large device scales (>10 $cm^2$) and high current densities (>200 mA $cm^{-2}$) haven't been extensively studied. Therefore, it is important to develop a deep understanding of how these $CO_2R$ pathways respond to different electrode compositions and operating conditions.

Often conflated, the electrocatalytic environment is not merely the nanoparticle or atomically dispersed macrocycle on which the reaction is said to occur, but more broadly encompasses the influence of the electrocatalyst, support, and, perhaps most critically, the electrolyte (be it liquid or in the form of an ionically conducting solid polymer, i.e., ionomer). For example, Verma et al.[21] reported significant changes in the FE of $CO_2R$ to CO when different electrolyte compositions were used in an electrochemical flow reactor. Rosen et al.[22] have shown that using an ionic liquid as the electrolyte can lower the initial reduction barrier and therefore improve the performance of $CO_2R$ to CO on Ag. It was also reported by Zhang et al.[23] that the pH at the surface of the cathode catalyst layer (CCL) plays a key role in defining the $CO_2R$ activity and efficiency. These responses all stem from the changes in the CCL environment caused by the electrolyte composition; Gupta et al.[24] demonstrated, via numerical modeling, that the concentrations of $H^+$, $CO_{2(aq)}$, $HCO_3^-$, and $CO_3^{2-}$ can all change significantly in the boundary layer near an electrode surface. $HCO_3^-$ was found to play an especially important role in $CO_2R$ reactions[25,26] and it was proposed by Wuttig et al.[27] and Zeng et al.[28] that $HCO_3^-$ can act as a kinetically relevant proton donor in $CO_2R$ pathways.

While GDEs have been extensively studied for fuel cells and water electrolyzers, they are a newer and less understood concept in $CO_2R$ cells. The catalyst layer on the GDE is usually composed of the catalyst, ionomer binder, and carbon support. Many studies have focused on direct modifications that can be made to the catalyst surface, which can alter the binding energies of various intermediate complexes, and consequently the selectivity of the material.[29–31] While the catalyst material can dictate the predominant reaction pathway(s) and inherent selectivity, the ionomer binder also plays a crucial role. In fuel cell GDEs, the binder can affect the ionic conductivity and the hydrophobicity of the catalyst layer as well as oxygen permeability.[32–34] However, in GDEs for $CO_2R$, the role of the binder material is not as clear due to the more complex ionic environment and multiple parallel reactions. Wang et al.[35] demonstrated that the addition of

PTFE led to improved $CO_2R$ efficiency, which they proposed was due to the enhancement of the electrochemically active surface area for $CO_2R$. It was also suggested by Lee et al.[36] that the functional groups on the polymeric binders can suppress the undesired HER, thereby providing more catalytic active sites for $CO_2R$. Similarly, Pan et al. showed that adding a Nafion overlayer to a Cu electrode can greatly enhance the $CO_2R$ to methane.[37] Ozden and coworkers[30] developed an hierarchical catalyst layer design with the ionomer interface improving both the local $CO_2$ availability and the adsorption of the key reaction intermediates. These indirect non-catalyst modification approaches are important to understand because they may be applied in parallel with direct surface enhancements.

The goal of this study was to determine valid approaches for controlling the selectivity of $CO_2R$ through modifications to the catalyst layer microenvironment. The previously mentioned works have detailed how the aqueous environment (i.e., the catholyte) can play a significant role in this regard. However, it is unlikely that supplying a catholyte is a sustainable long-term solution for ostensibly gas fed cells. Therefore, in this work we chose to primarily employ on a non-buffering catholyte ($K_2SO_4$) to focus on strategies relevant to the operation of entirely gas fed cells, which must rely on changes to the solid-state components to control selectivity. To some extent, the effects of a buffering catholyte ($KHCO_3$) were also studied, but this was mainly to gain insight about the reaction pathways.

In this work, we combine both experimental and theoretical analyses to investigate the factors affecting the FE of a $CO_2$ electrolysis cell. Specifically, different catalysts, binder materials, and catholyte compositions are studied. The FE of the cell is measured experimentally under varying conditions to understand their impact on the branching ratios of the two-electron $CO_2R$ products. As a complimentary effort, a 2D multiphysics transport model is developed and used to elucidate the fundamental process occurring in the cathode electrode. Multiphysics modeling is a useful tool for complex systems like this because they can help visualize and deconvolute the micro-scale phenomena that are difficult to observe experimentally. Our results show that the selectivity of Ag, a CO-forming catalyst, can change significantly when different catholyte compositions and binder materials are used. In contrast, the selectivity of $SnO_2$, a $HCOO^-$-forming catalyst, is relatively stable across the conditions studied. These insights can be used to inform decisions regarding electrode architecture and operating conditions, and ultimately contribute to the scaling up of electrochemical $CO_2R$ devices.

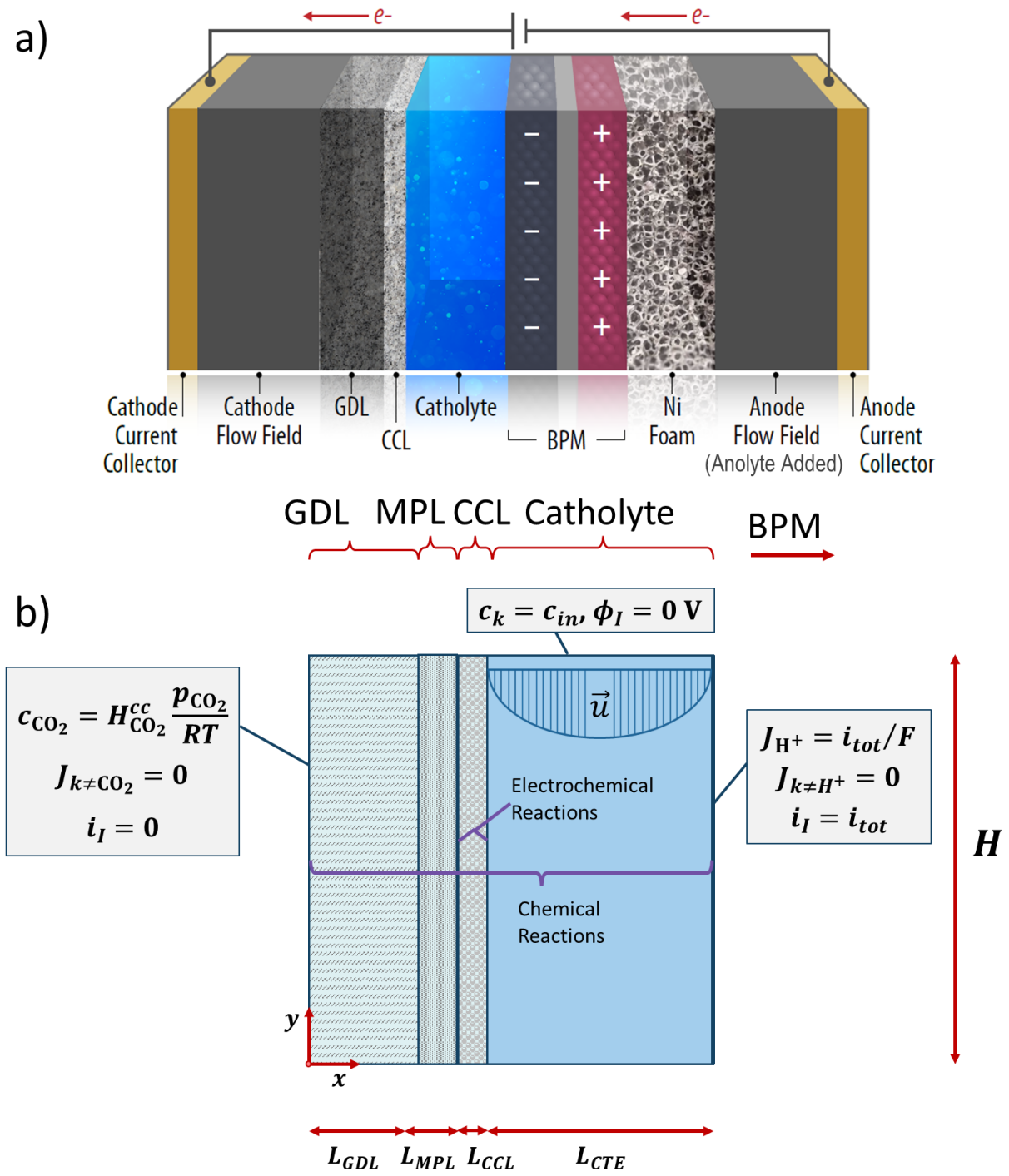


Figure 1 – Schematics of a) the experimental $CO_2R$ device, and b) the 2D model geometry and selected boundary conditions in the region of the cathode electrode and the catholyte layer.

## 2. Experimental Methods

### *2.1 Cathode Preparation*

The cathode catalyst inks were prepared by mixing commercial catalyst materials supported on Vulcan carbon ("Vu", XC-72R, Fuel Cell Store), isopropanol alcohol (HPLC Plus grade 99.9%, Sigma Aldrich), deionized (DI) water (18 MΩ-cm), and binder. Three different binder materials were tested in this study: 5 wt. % Nafion ionomer (1100 EW, Ion Power), 10 wt. % perfluorinated anion exchange (PFAEM) ionomer[38], and 60 wt. % polytetrafluoroethylene (PTFE, Teflon™ PTFE DISP 30 Fluoropolymer dispersion, Chemours). Two commercial catalysts were studied: 40% Ag/Vu (30 nm average diameter, Fuel Cell Store), and $SnO_2$ nanoparticles (< 100 nm diameter, Sigma Aldrich). For all $SnO_2$ electrodes, a 1:1 ratio of $SnO_2$ to Vulcan was used. In all inks the ratio of binder:carbon was fixed at 3:5, and the solvent ratio of DI water:isopropanol was fixed at 2:3 to ensure fair comparison of electrochemical metrics.

The catalyst ink was first dispersed using a horn sonicator (three times, 30s each time) and an ice bath sonicator (60 min), and then hand-painted onto the microporous layer (MPL) side of the GDL (Sigracet 39BC, Fuel Cell Store) on a heated vacuum table at 95°C. The GDE was then hot annealed at 120°C for 2 hours. Catalyst loadings of 0.1 mg $cm^{-2}$ and 0.5 mg $cm^{-2}$ were used, which were determined using the difference in mass before/after. Each batch of ink was used to make four electrodes, and the loading differences between batches were all within 10%. In this manuscript, all experimental data shown represent the average of three independent tests, each time with a new cell (new electrodes, new membrane, fresh electrolytes) which all showed good repeatability.

These catalyst materials were intentionally chosen as standard, commercially available materials, to allow focus on subsequent changes to the microenvironment that can be made. Other studies have characterized the role of chemistry and surface structure of $Sn/SnO_2$[39–41] and Ag[42–44] materials in much more detail. We envision our efforts herein to be used in parallel with surface modification and other chemistry approaches.

### *2.2 Electrochemical Testing*

Figure 1a shows a sketch of the square 25 $cm^2$ cell used for measuring the electrochemical performance of different cathode GDEs in this study. Ni foam (MFNi16m, MTI Corporation) was used as the anode. A bipolar membrane (BPM) (FBM, Fumatech GmbH, Fuel Cell Store) was placed with the anion exchange layer (AEL) next to the Ni foam and with the cation exchange layer (CEL) facing the cathode side. A "Z" shaped catholyte chamber of 1.27 mm thickness (Figure

S1) was used between the BPM and cathode GDE. The anode and cathode were compressed by 9% and 18%, respectively, following tightening of the cell to 40 inch-pounds.

Four different catholyte compositions were used during operation, as detailed in Table 1. 1 M KOH was used as anolyte, which was fed to the cell via the anode flow field. The catholyte solutions were made by dissolving $K_2SO_4$ powder, and $KHCO_3$ (all materials Certified ACS, VWR) in 18 MΩ cm DI water. *1 M KOH and 1 M $H_2SO_4$ solutions were added to adjust the pH to the desired value shown in Table 1*.

**Table 1.** Catholyte compositions studied in this work.

| # | $K_2SO_4$ | $KHCO_3$ | Inlet pH |
|---|---|---|---|
| 1 | 0.4 M | 0 | 7 |
| 2 | 0.4 M | 0 | 10 |
| 3 | 0.4 M | 0.08 M | 7 |
| 4 | 0.4 M | 0.08 M | 10 |

During operation, the cell, $CO_2$ gas feed, and anolyte were all heated to 60°C. The anolyte was fed to the triple serpentine anode flow field at 50 ml $min^{-1}$ and the catholyte was fed to the catholyte chamber at 40 ml $min^{-1}$. $CO_2$ was fed to the triple serpentine cathode flow field at 2 L $min^{-1}$ and ambient pressure (approximately 83.36 kPa in Golden, CO).

A Gamry Reference 3000 potentiostat with a Reference 30k Booster was used to conduct galvanodynamic polarizations at 1 mA $cm^{-2}$ $s^{-1}$. Gas and liquid samples were obtained from the cathode after the cell was held at constant current densities for one minute. The gas samples were collected in gas bags (Supel™-Inert multi-layer foil, Sigma Aldrich) and were analyzed in a 4900 Micro gas chromatograph (GC, 10 m, molecular sieve, Agilent). The liquid samples were diluted to 25 ml with 18 MΩ cm DI water, filtered with PTFE 0.22 µm syringe filters, and then analyzed using high-performance liquid chromatography (HPLC, 1260 Infinity II Bio-inert, Agilent) with an Aminex HPX-87H column. 4 mM sulfuric acid ($H_2SO_4$) flowing at 0.6 ml/min was used as the mobile phase. For additional details, see Chen et al. 2020.[12]

## 3. Mathematical Model

### *3.1 Overview*

A mathematical model was developed to study the species transport, electrochemistry, and multiphase phenomena of the cathode GDE during operation. A full description of the model is given in the Supporting Information (SI), Section S.2, and a high-level description is provided here. A schematic of the model geometry and boundary conditions is presented in Figure 1.

The system is solved for the concentrations of ten aqueous species ($CO_{2(aq)}$, $H^+$, $OH^-$, $HCO_3^-$, $CO_3^{2-}$, HCOOH, $HCOO^-$, $K^+$, $HSO_4^-$, and $SO_4^{2-}$), three gaseous species ($CO_{2(g)}$, $H_2$, and CO), liquid and gas phase pressures ($p_L$ and $p_G$, respectively), and the electrostatic potential ($\phi_I$). The species transport and the electrostatic potential were modeled using the Poisson-Nernst-Planck (PNP) system of equations, i.e., the electroneutrality condition was not implemented as an explicit assumption. This approach allowed us to directly model the Donnan exclusion effect at the GDL|CCL and CCL|catholyte boundaries. Furthermore, this provided a relatively simple approach for studying the effect of different ionomer materials. The main difference between the binder materials is the sign of the fixed charge groups: the PFAEM binder features positive fixed charges, the Nafion binder features negative charges, and the PTFE binder has no fixed charges. Using the PNP approach allows for simple and direct simulation of this effect. Other assumptions used in the model development are as follows:

- Dilute solution theory is used to model the aqueous species transport. While concentration solution theory would more accurately account for the various ion-ion interactions, there are too many unknown parameters to implement it here.
- Computational domains are limited to the GDL, CCL, and catholyte; the BPM and anode components are not modeled. At the catholyte|BPM interface, the ionic current is assumed to be supplied entirely by protons while the fluxes of all other ions are set to zero. During operation, water dissociation at the CEL|AEL interface of the BPM serves as a source of protons whose flux is proportional to the total current. While the flux of other supporting ions is likely not exactly zero at the catholyte|BPM interface, this assumption serves as a reasonable approximation for observing the $H^+$ boundary layer that develops at this interface.
- The velocity field in the catholyte domain is assumed to correspond to the solution for fully developed incompressible flow between two flat plates. This is an idealization, as the actual flow field varies in 3D due to the Z-shaped gasket that defines the gap between the GDE and the BPM. A direct Navier Stokes simulation of the 3D flow field is shown in the SI,

Figure S2. The 2D flat plates solution is computationally efficient and allows us to observe fundamental effects such as chemical reactions within the boundary layer, as well as combined species transport due to diffusion, migration, and convection.

### *3.2 Electrochemical Reactions*

Electrochemical $CO_2$ reduction is a complicated process that features several intermediate species and multiple final products. On Ag/Vu and $SnO_2$/Vu catalysts, the proton can be donated by $HCO_3^-$, $H_2O$, $H_3O^+$ ($H^+$), and/or $H^{\bullet}_{(ad)}$.[45] The overall reactions for CO and $HCOO^-$ formation for the different proton sources are given by Eqs. (1) – (7) (proposed mechanisms using elementary steps are shown in the SI, Section S.3). The standard potentials for the reactions are also shown and are calculated using the free energies of formation for each species. Note that the standard potentials reported here use the free energy of formation for aqueous $CO_2$, rather than gaseous, to coincide with the current understanding of the mechanisms in the literature. Clearly, the proton source can significantly change the performance of a catalyst. If no free protons are readily available, then $CO_2$ reduction must use $HCO_3^-$ or $H_2O$ as the proton source, which requires more negative potentials. However, an abundance of free protons may facilitate the acidic HER, Eq. (8), thereby lowering the FE to non-$H_2$ products.

| **CO:** | $E^0$ (V $vs.$ SHE) | |
|---|---|---|
| $CO_{2(aq)} + 2H^+ + 2e^- \rightleftharpoons CO + H_2O$ | $-0.061$ | (1) |
| $CO_{2(aq)} + 2HCO_3^- + 2e^- \rightleftharpoons CO + H_2O + 2CO_3^{2-}$ | $-0.673$ | (2) |
| $CO_{2(aq)} + HCO_3^- + 2e^- \rightleftharpoons CO + OH^- + CO_3^{2-}$ | $-0.781$ | (3) |
| $CO_{2(aq)} + H_2O + 2e^- \rightleftharpoons CO + 2OH^-$ | $-0.889$ | (4) |
| **$HCOO^-$:** | | |
| $CO_{2(aq)} + H^+ + 2e^- \rightleftharpoons HCOO^-$ | $-0.160$ | (5) |
| $CO_{2(aq)} + HCO_3^- + 2e^- \rightleftharpoons HCOO^- + CO_3^{2-}$ | $-0.466$ | (6) |
| $CO_{2(aq)} + H_2O + 2e^- \rightleftharpoons HCOO^- + OH^-$ | $-0.574$ | (7) |
| **HER:** | | |
| $2H^+ + 2e^- \rightleftharpoons H_2$ | $-0.0$ | (8) |
| $2H_2O + 2e^- \rightleftharpoons H_2 + 2OH^-$ | $-0.828$ | (9) |

The above proposed $CO_2R$ pathways proceed via many of the same or similar intermediate species, so the overall production rates are likely comprised of some combination of all the above reactions. However, to model the $CO_2R$ reactions, a single pathway was assumed for each reaction. In addition, many of the kinetic parameters for these reactions are still unknown, so assuming a single reaction for each product reduces the number of fitting parameters. In this work, the electrochemical reactions are modeled using Butler-Volmer kinetics, as shown in Eqs. (10) – (13) (subscripts for the transfer coefficients are omitted to save space). Other, more complicated multi-step mechanisms can be developed for $CO_2R$, for instance that of Singh et al.[46], however these require specialized experiments and first principles studies.

Our experimental work, described later, has shown that the kinetics of the $CO$ forming reaction on Ag/Vu improve as the pH of the buffer solution is increased. Verma et al.[47] noted similar trends: the highest FEs to CO were observed when using the highest concentrations of KOH and $KHCO_3^-$. These results suggest that neither $H_3O^+$ nor $H^{\bullet}_{(ad)}$ are the likely proton donors, leaving $H_2O$ and $HCO_3^-$ as the most likely candidates. These two pathways (Eqs. (2) and (4)) are investigated in this work and the two Butler-Volmer kinetic expressions are shown in Eqs. (11) and (12). Hatsukade et al. presented a Tafel analysis that suggested that the mechanism for $CO$ production on $Ag/Vu$ may change when moving from low to high overpotentials, which would require a modification to our approach involving single Butler-Volmer reactions. However, their mechanism development assumed that $H_3O^+$ are abundant enough to be the sole proton donor for the $CO$ pathway, which was determined to be unsuitable for the conditions studied in this work (i.e., that assumption would lead to observed mass transport limitations in the model). Therefore, while the single Butler-Volmer expressions are likely an oversimplification of the $CO_2R$ mechanism, they still allow us to observe the relevant mass transport phenomena occurring in the GDE and catholyte.

On $SnO_2$/Vu, we assume that $HCO_3^-$ is the proton donor for the $HCOO^-$ reaction because the literature is in more agreement about this point[45]. For example, Zhang et al. have reported that the $CO_2R$ to $HCOO^-$ exhibits a first-order dependence on $HCO_3^-$ concentration on $SnO_2$ nanoparticles[48], which is captured by Eqs. (6) and (13). Overall, our approach is similar to the modeling works of Weng et al.[49,50] and Kas et al.,[51] except that we extend the electrochemical model to include both $CO_2R$ pathways on each catalyst material (Ag/Vu and $SnO_2$/Vu).

$$i_{HER} = i_{0,HER}\left(\left(\frac{p_{H_2}}{p^0_{H_2}}\right)\left(\frac{c_{OH^-}}{c^0_{OH^-}}\right)^2 \exp\left(\frac{\alpha_a F}{RT}\eta_{HER}\right) - \exp\left(-\frac{\alpha_c F}{RT}\eta_{HER}\right)\right) \quad (10)$$

$$i_{CO} = i_{0,CO}\left(\left(\frac{p_{CO}}{p^0_{CO}}\right)\left(\frac{c_{CO_3^{2-}}}{c^0_{CO_3^{2-}}}\right)^2 \exp\left(\frac{\alpha_a F}{RT}\eta_{CO}\right) - \left(\frac{c_{CO_2}}{c^0_{CO_2}}\right)\left(\frac{c_{HCO_3^-}}{c^0_{HCO_3^-}}\right)^2 \exp\left(-\frac{\alpha_c F}{RT}\eta_{CO}\right)\right) \quad (11)$$

$$i_{CO} = i_{0,CO}\left(\left(\frac{p_{CO}}{p^0_{CO}}\right)\left(\frac{c_{OH^-}}{c^0_{OH^-}}\right)^2 \exp\left(\frac{\alpha_a F}{RT}\eta_{CO}\right) - \left(\frac{c_{CO_2}}{c^0_{CO_2}}\right)\exp\left(-\frac{\alpha_c F}{RT}\eta_{CO}\right)\right) \quad (12)$$

$$i_{HCOO^-} = i_{0,HCOO^-}\left(\left(\frac{c_{HCOO^-}}{c^0_{HCOO^-}}\right)\left(\frac{c_{CO_3^{2-}}}{c^0_{CO_3^{2-}}}\right)\exp\left(\frac{\alpha_a F}{RT}\eta_{HCOO^-}\right) - \left(\frac{c_{CO_2}}{c^0_{CO_2}}\right)\left(\frac{c_{HCO_3^-}}{c^0_{HCO_3^-}}\right)\exp\left(-\frac{\alpha_c F}{RT}\eta_{HCOO^-}\right)\right) \quad (13)$$

## 4. Results and Discussion

The first two Results and Discussion sections will present the effects of catholyte composition and binder material on the selectivity of the $CO_2R$ on Ag/Vu and $SnO_2$/Vu catalyst materials. Where appropriate, modeling results will be tied in to better understand the mechanisms behind the observed changes in the FE. The last section will use the results of the model to visualize and glean information regarding transport phenomena occurring within the cathode components. The motivation for these investigations is to determine possible avenues beyond catalyst approaches to dictate the local catalyst environment, leading to higher selectivity toward $CO_2R$ products. These indirect methods may then be used in conjunction with other efforts that seek to directly modify the catalyst surface.

### *4.1 Catholyte Composition*

Figure 2 shows the effect of catholyte composition on the $CO_2R$ product distribution as a function of current density. As noted in Table 1, four catholyte compositions were studied: *(i)* 0.4 M $K_2SO_4$, pH = 7, *(ii)* 0.4 M $K_2SO_4$, pH = 10, *(iii)* 0.4 M $K_2SO_4$ + 0.08 M $KHCO_3$, pH = 7, and *(iv)* 0.4 M $K_2SO_4$ + 0.08 M $KHCO_3$, pH = 10. In all tests, a Nafion binder and catalyst loading of 0.5 mg cm$^{-2}$ were used.

Figure 2a shows that for Ag/Vu catalysts, adding $KHCO_3$ to the catholyte results in higher non-$H_2$ FE than the tests with no $KHCO_3$. At pH = 7, adding just 0.08 M $KHCO_3$ to the 0.4 M $K_2SO_4$ catholyte improved the non-$H_2$ FE by about 200%. Similarly, at pH = 10, the non-

$H_2$ FE was ~170% higher with the $KHCO_3$ buffered catholyte than the non-buffered catholyte. Figure 2b demonstrates how the Ag/Vu catalyst primarily produces CO instead of $HCOO^-$. By breaking down the non-$H_2$ FE into contributions from CO and $HCOO^-$, it is evident that the CO pathway contributes to the major differences in non-$H_2$ FE, while the $HCOO^-$ pathway was barely affected. Not only do these trends reveal the most effective chemistries with which to operate the cell, but they also provide insight to the $CO_2R$ mechanism on Ag. Improved selectivity to CO occurs both when adding $KHCO_3$ and when increasing the pH of the catholyte; both actions increase the concentration of $HCO_3^-$ in the solution (more $CO_2$ is converted to $HCO_3^-$ as the pH is increased), which may play an active role in $CO_2R$ to CO pathway. This phenomenon will be explored and discussed further using the modeling results. These results corroborate the observations reported by Verma et al.[47] while also reporting the activity of Ag/Vu for the $HCOO^-$ pathway.

Figure 2c shows that on $SnO_2$/Vu, the total non-$H_2$ FE is above 90% for almost all current densities and catholytes. While $SnO_2$ primarily favors the $HCOO^-$ pathway, it also produces a moderate amount of CO, as shown in Figure 2d. On $SnO_2$/Vu, the CO pathway was again more affected by the catholyte composition than the $HCOO^-$ pathway. At 500 mA $cm^{-2}$, the FE of the CO pathway was improved by 2.7 times using the $0.4\ M\ K_2SO_4 + 0.08\ M\ KHCO_3, pH = 10$ catholyte, while the change in the $HCOO^-$ pathway was within 10%. This resulted in an increase in the total non-$H_2$ FE, which remained above 90% for all catholytes.

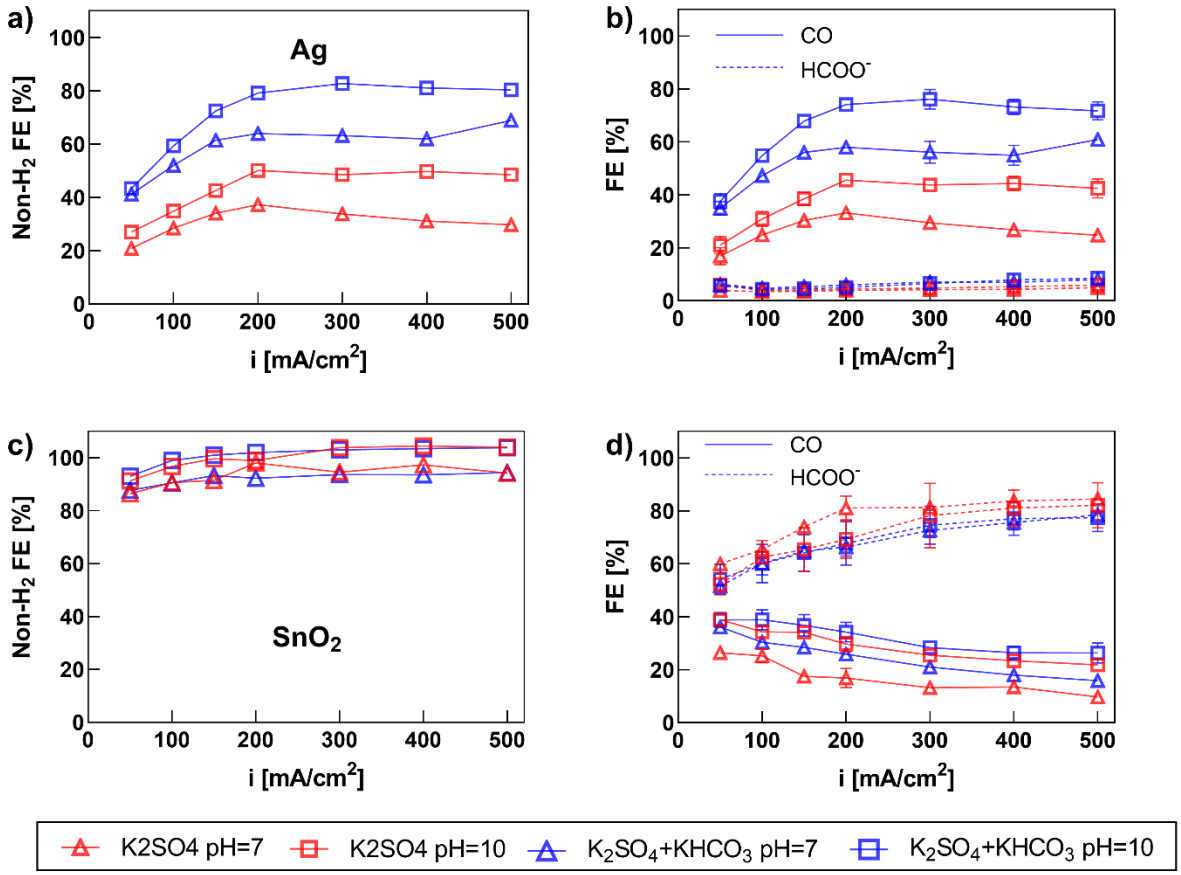


*Figure 2 – a) Total non-$H_2$ FE and b) individual FE to CO and $HCOO^-$ obtained as a function of the current densities in different catholytes with Ag/Vu electrodes; c) total non-$H_2$ FE and d) individual FE to CO and $HCOO^-$ tested with $SnO_2$/Vu electrodes. In b) and d) the solid lines represent FE to CO and the dashed lines represent the FE to $HCOO^-$. For all tests, the catalyst loading was 0.5 mg cm$^{-2}$ and Nafion ionomer binder was used in the catalyst layer. The cell was operated at 60$^o$C and the catholytes were fed to the cell at 40 ml min$^{-1}$.*

The results in Figure 2 reveal that with both Ag/Vu and $SnO_2$/Vu electrodes, the production of CO is more sensitive than $HCOO^-$ to the change of catholyte compositions. The main differences in the catholyte compositions tested here are the solution pH and $HCO_3^-$ concentrations. Figure 3 demonstrates how the transport model was used to investigate the mechanism of the $CO_2R$ on Ag. After reviewing the literature, the choice of proton donor for the CO pathway was narrowed down to be either $HCO_3^-$ or $H_2O$ (Eqs. (2) and (4), respectively). Using the 0.4 M $K_2SO_4$ electrolyte as a baseline, the exchange currents and transfer coefficients in Eqs. (11) and (13) were manually tuned until the model showed good agreement to the experimental data. The results of this process are shown in Figure 3a and Figure 3c for proton donors of $H_2O$ and $HCO_3^-$,

respectively, and the fitted parameters are listed in Table 2. The formate pathway accounts for just a small fraction of the total current on Ag/Vu and is not discussed much in the literature, so it was assumed to proceed via Eq. (7).

**Table 2.** Fitted kinetic parameters used to study the $CO_2R$ pathways.

| Parameter | Value | |
|---|---|---|
| | **Ag** | **$SnO_2$** |
| *HER, acidic pathway* | | |
| $i_0$ (A m$^{-2}$) | $9.0 \times 10^{-1}$ | $1.0 \times 10^{-2}$ |
| $\alpha_c$ | 0.5 | 0.5 |
| *HER, alkaline pathway* | | |
| $i_0$ (A m$^{-2}$) | $2.0 \times 10^{-2}$ | $1.0 \times 10^{-3}$ |
| $\alpha_c$ | 0.33 | 0.3 |
| *$CO_2R$ to CO* | | |
| $i_0$ (A m$^{-2}$) | $9.0 \times 10^{-3}$ | $1.0 \times 10^{-2}$ |
| $\alpha_c$ | 0.4 | 0.5 |
| *$CO_2R$ to $HCOO^-$* | | |
| $i_0$ (A m$^{-2}$) | $2.0 \times 10^{-6}$ | $8.0 \times 10^{-5}$ |
| $\alpha_c$ | 0.43 | 0.5 |

Next, without changing the obtained kinetic parameters, the catholyte inlet condition was changed in the model to reflect the 0.4 M $K_2SO_4$ + 0.08 M $KHCO_3$ composition. The resulting simulated partial current densities (dashed lines) are shown in Figure 3b and Figure 3d. When $H_2O$ is assumed to be the proton donor for CO pathway, there is no significant change in the partial currents when $HCO_3^-$ is added to the catholyte. This is a stark deviation from the experimental data, which suggests that this assumed mechanism ($H_2O$ as the proton donor) is not sufficient to capture the observed trends. However, when $HCO_3^-$ is assumed to be the proton donor for the CO pathway, the model captures the changing experimental trend that $i_{CO}$ increases as $HCO_3^-$ is added to the catholyte. In this way, the transport model was able to suggest the likely proton donors for each

$CO_2R$ pathway on Ag: $H_2O$ for the $HCOO^-$ pathway and $HCO_3^-$ for the CO pathway. These proton donors were used in all subsequent modeling results presented in this work.

It should be noted that the overall $CO_2R$ reaction proceeds via many simultaneous elementary steps involving similar intermediate species. Therefore, a single Butler-Volmer equation representing each partial current is likely an oversimplification. However, as demonstrated in Figure 3, it can be a useful tool for investigating the effects of mass transport on the performance of an electrode. Regardless of the microkinetic steps, the overall species production rates are tied to the partial current densities, which are accounted for in this modeling approach. We hope that these results encourage future studies on these materials across an even broader range of operating chemistries.

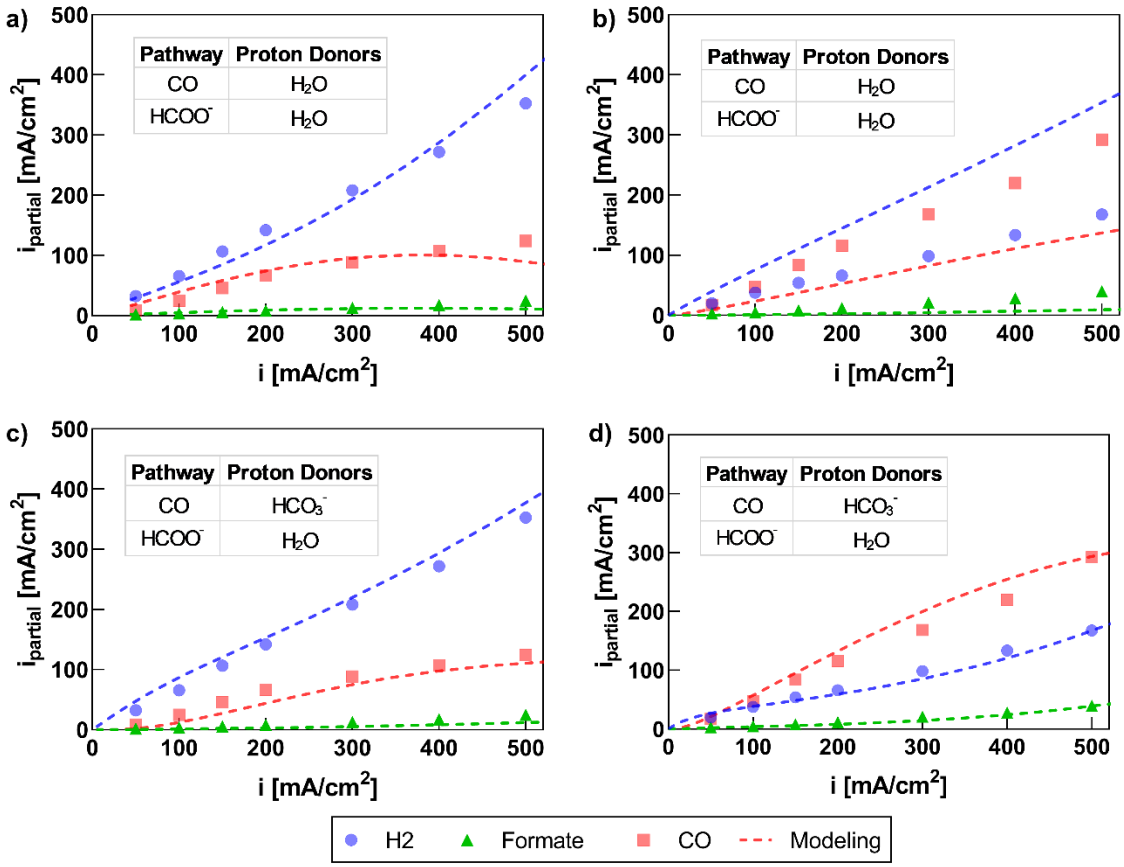


*Figure 3 – Comparison of the tuned model to experimental data using Ag as the cathode catalyst material. The top row assumes that $H_2O$ is the proton donor for $CO_2R$ to both $CO$ and $HCOO^-$ and features a) 0.4 $M$ $K_2SO_4$ as the catholyte and b) 0.4 $M$ $K_2SO_4$ + 0.08 $M$ $KHCO_3$ as the catholyte. The bottom row assumes that $HCO_3^-$ is the proton donor for $CO_2R$ to $CO$ and $H_2O$ is*

*the proton donor for $CO_2R$ to $HCOO^-$ and features c) 0.4 M $K_2SO_4$ as the catholyte and d) 0.4 M $K_2SO_4$ + 0.08 M $KHCO_3$ as the catholyte. For all tests, the Ag/Vu loading was 0.5 mg cm$^{-2}$ and Nafion ionomer binder was used in the catalyst layer. The cell was operated at 60°C and the catholytes were fed to the cell at 40 ml min$^{-1}$.*

A similar technique was employed to fit the kinetic parameters for the $SnO_2$/Vu catalyst. Figure 4a shows the fitted results for the baseline 0.4 M $K_2SO_4$ catholyte chemistry, and Figure 4b shows the results using the 0.4 M $K_2SO_4$ + 0.08 M $KHCO_3$ catholyte. The fitted parameters, listed in Table 2, illustrate the delicate balance between kinetics and thermodynamics. On $SnO_2$, the kinetics of the $HCOO^-$ pathway are more facile compared to Ag, which allows the thermodynamic differences to dominate the catalyst's performance. For example, on $SnO_2$, the exchange current density of the CO pathway is more than 10 times greater than the $HCOO^-$ pathway, but the equilibrium potential for the $HCOO^-$ pathway is about 200 mV less negative. This leads to the effects observed in Figure 4 due to the nature of the Butler-Volmer kinetic model: while the exchange current densities provide a linear scaling effect, the overpotentials contribute to the exponential terms. Any cathode potential negative enough to drive appreciable HER or CO currents would result in a far greater overpotential for the $HCOO^-$ pathway. This is also why little benefit is observed upon switching to the catholyte containing $HCO_3^-$, even though $HCO_3^-$ is the assumed proton donor in the model.

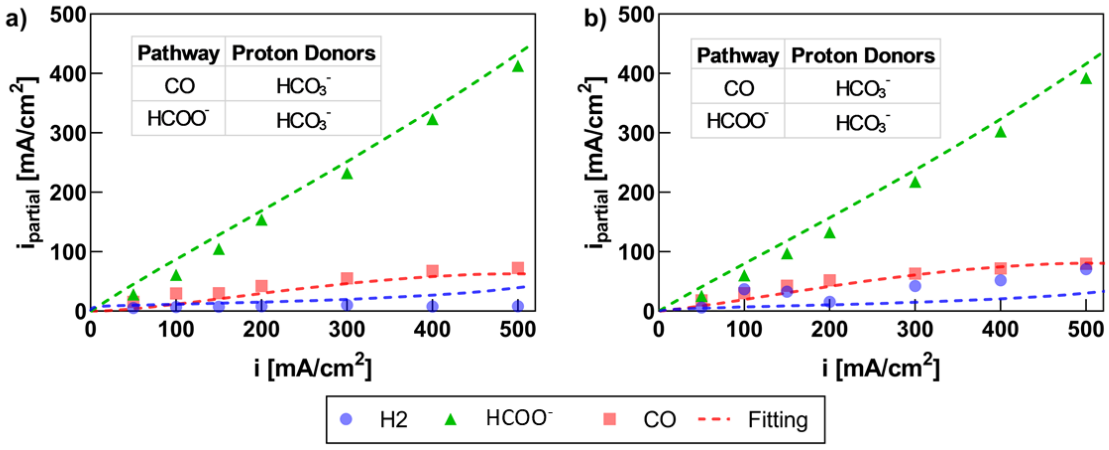


*Figure 4 – Comparison of the tuned model to experimental data using $SnO_2$ as the cathode catalyst material featuring a) 0.4 M $K_2SO_4$ as the catholyte and b) 0.4 M $K_2SO_4$ + 0.08 M $KHCO_3$ as the catholyte. The proton donor for $CO_2R$ to both $CO$ and $HCOO^-$ is assumed to be $H_2O$. For all tests, the catalyst loading was 0.5 mg cm$^{-2}$ and Nafion ionomer binder was*

*used in the catalyst layer. The cell was operated at 60°C and the catholytes were fed to the cell at 40 ml min$^{-1}$.*

### *4.2 Binder Material*

While most of the research in $CO_2R$ field has been focused on the catalyst development and modification, the role of the binder material in the catalyst layer is often neglected and less understood. It was proposed in the literature that the addition of the binders in the catalyst layer can improve the local $CO_2$ availability and provide more catalytic active sites for $CO_2R$.[30,35,36] However, few systematic investigations with ionomer binders of different fixed charges have been performed.

Figure 5 shows the effect of the ionomer binder on the product distribution of Ag/Vu and $SnO_2$/Vu catalysts using the $0.4\ M\ K_2SO_4, pH = 7$ catholyte. The main difference between each binder material is the sign of the fixed charges, with the notable difference that the PTFE binder is also significantly more hydrophobic than Nafion or PFAEM. PFAEM is a perfluorinated anion exchange polymer with high levels of ion exchange and membrane conductivity.[52] The sign of the fixed charges dictates which ions are the most prevalent in the CCL. With the PFAEM binder, this means higher concentrations of $HCO_3^-$, $CO_3^{2-}$, $HSO_4^-$, $SO_4^{2-}$, and $HCOO^-$; with the Nafion binder this means higher concentrations of $K^+$ and $H^+$.

Figure 5a shows that, in the Ag/Vu electrodes, nearly 100% FE to CO was obtained when using the PFAEM binder. In contrast, less than 30% FE to CO was obtained using the Nafion binder. The choice of binder was not found to have any significant effect on the FE to $HCOO^-$, as shown in Figure 5b. This means that the difference in performance is mostly attributable to a change in the $H_2$ production, with Nafion producing much more $H_2$. This suggests that the CO and HER reactions are competitive and sensitive to changes in the local environment, while the activity of the $HCOO^-$ pathway is much less (though nonzero). If the kinetics of the $HCOO^-$ pathway were comparable to the CO and HER reactions in the Ag/Vu electrodes, then the FE to $HCOO^-$ would see a similar increase using Nafion compared to PFAEM. In addition, although Nafion is typically thought of as an acidic environment, there are not enough free $H^+$ for the acidic HER to proceed as shown in Eq. (8); the HER competing with CO production is assumed to proceed via Eq. (9). That is not to say that there is not a more nuanced HER pathway that takes adsorbed $H^{\bullet}_{(ad)}$ from

the $CO_2R$ process. This could be another mechanism for these reactions to compete and should be reconciled in future microkinetic studies.

The product distributions for $SnO_2$/Vu follow similar trends, but with smaller variations in performance. The FE to CO, shown in Figure 5c, is highest using PTFE and lowest using Nafion, but generally comprising 10%-20% of the overall FE at 500 mA/cm$^2$. Figure 5d shows that similar amounts of $HCOO^-$ are made with Nafion and PFAEM binder, while PTFE shows slightly less FE to $HCOO^-$. In general, however, the performance of $SnO_2$/Vu with different binders is relatively consistent compared to the variations observed using Ag. This means that the kinetics of the $HCOO^-$ pathway on $SnO_2$ are facile enough to allow the effect of its higher thermodynamic potential to dominate the performance. The results of Figure 5 also demonstrate that, in general, the production rate of CO is more sensitive to the local environment than $HCOO^-$ using both Ag/Vu and $SnO_2$/Vu electrodes.

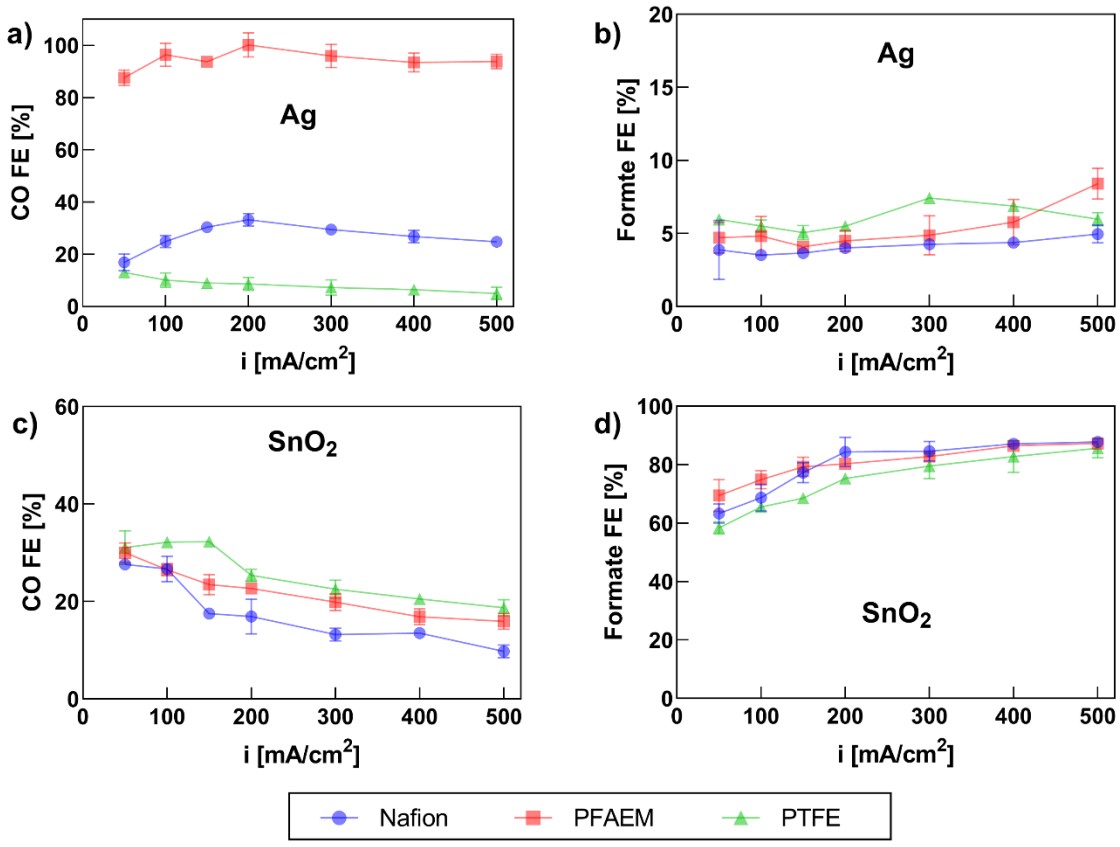


*Figure 5 – FE of the a) CO and b) $HCOO^-$ pathways as a function of current density using Ag, as well as the FE of the c) CO and d) $HCOO^-$ pathways using $SnO_2$/Vu. Different ionomer*

*binders were used in the catalyst layer: Nafion, PFAEM, and PTFE. The catalyst loading for Ag/Vu and $SnO_2$/Vu was 0.5 mg $cm^{-2}$, and 0.4 $M\ K_2SO_4, pH = 7$ was used as the catholyte. The cell was operated at 60°C and the catholytes were fed to the cell at 40 ml $min^{-1}$.*

The results of Figure 2 – Figure 5 show that the CO partial current density is the most sensitive to changes in the local environment with either Ag/Vu or $SnO_2$/Vu catalyst. In particular, the prevalence of local $HCO_3^-$ appears to be a key factor. Adding $KHCO_3$ directly increases the $HCO_3^-$ content, while raising the pH of the catholyte also has the indirect effect of also increasing the equilibrium concentration of $HCO_3^-$ (up to about $pH = 10$).[29] In addition, there should be higher $HCO_3^-$ concentrations in the electrodes with PFAEM binder compared to that with Nafion binder. These three effects all combine to control the electrochemical microenvironment near the electrocatalyst surface. The additional presence of $HCO_3^-$ in the catholyte results in more $HCO_3^-$ in the catalyst layer. Although Nafion tends to repel anions, the aqueous ionic environment is strong enough to lower the permselectivity of the Nafion resulting in anions "leaking" into this layer. In contrast, the PFAEM binder tends to attract anions into the catalyst layer which naturally raises the local concentration of $HCO_3^-$. As discussed before, the proton donor for CO pathway on Ag/Vu catalyst is proposed to be $HCO_3^-$. This analysis explains the higher rates of CO production with the PFAEM ionomer shown in Figure 5a.

To verify and demonstrate these points, the model was used to interrogate species concentrations in the catalyst layer. First, the model was used to compute the partial current densities of the primary $CO_2R$ products using different binders. These results are shown in Figure 6a for Ag/Vu and Figure 6b for $SnO_2$/Vu, and include experimental data for further validation. The model captures the changing trends in CO production on Ag, while also confirming the relatively constant rate of $HCOO^-$ production on $SnO_2$. It should be noted that the agreement of the model with the experimental data is not as good for the Ag:PTFE data as it is for the other binder materials. It is possible that PTFE changes the free energies associated with the elementary steps in ways that are not accounted for here. Another possibility is that the catalyst layer has a significantly different morphological properties, such as electrochemically active surface area or agglomerate structure that alters accessibility and electrocatalyst utilization. These properties were not able to be characterized for the present study, but remain an interesting area for future work, especially because the binder material has such a significant effect on the selectivity of Ag.

The extrinsic catalyst layer species distributions of $HCO_3^-$ and $CO_{2(aq)}$ at different current densities are shown in Figure 6c and Figure 6d, respectively. The extrinsic concentration refers to the number of moles per unit volume of catalyst layer (as opposed to moles per unit volume of solvent). In other words, the extrinsic concentrations include the effect of the local liquid water volume fraction. Figure 6c shows that the PFAEM CCL has a higher local concentration of $HCO_3^-$ than the Nafion. The PTFE binder has the lowest $HCO_3^-$ concentration, and hence the lowest $i_{CO}$, mainly because of its hydrophobicity. These trends in $HCO_3^-$ concentrations are consistent with the trends in the experimental $i_{CO}$ in Figure 6a and it further confirms the previous discussion that $HCO_3^-$ plays an important role in the pathway of $CO_2R$ to CO on Ag.

The aqueous $CO_2$ concentration profiles are shown in Figure 6d. According to the mechanisms reported in the literature, the $CO_2R$ reactions proceed using aqueous $CO_2$, which is less abundant if the volume fraction of water in the CCL is low. Therefore, while it is important to have a hydrophobic GDL to allow gaseous $CO_2$ access to the catalyst layer, it is also important to have hydrophilic catalyst layers to allow for $CO_2$ absorption and high local concentrations of reactants.

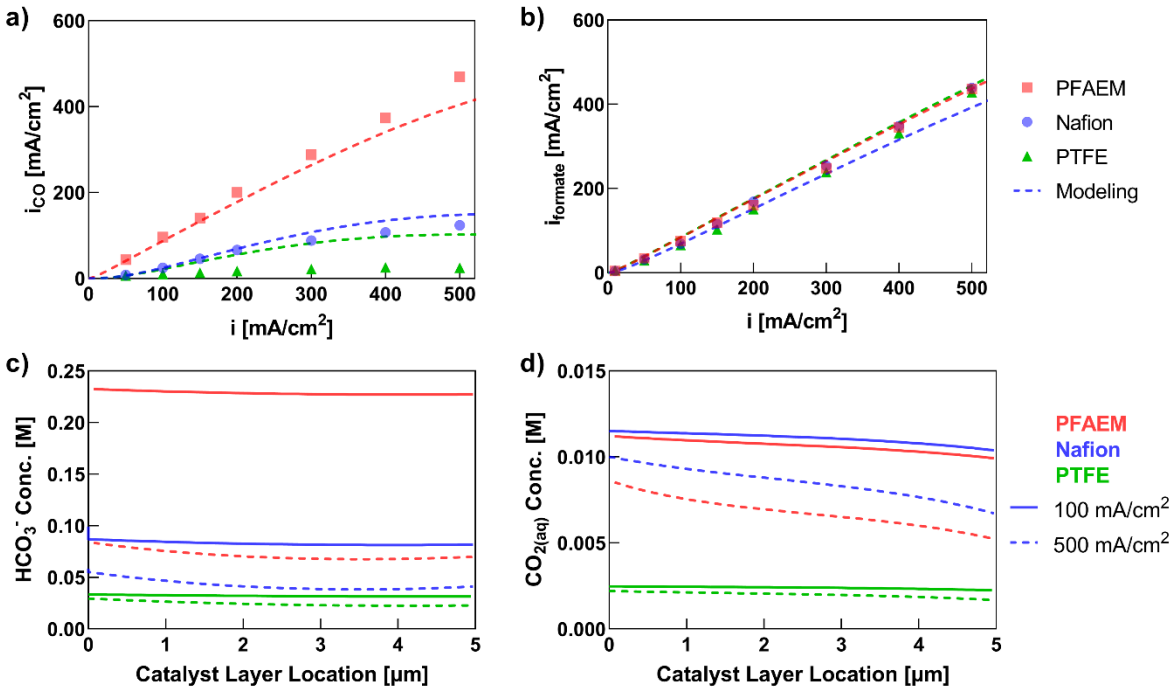

*Figure 6 – Comparison of the tuned model to experimental data of the partial current densities of the $CO_2R$ to a) $CO$ on Ag/Vu catalyst and b) $HCOO^-$ on $SnO_2$ catalyst using different binder materials: Nafion, PFAEM, and PTFE. The catalyst loading for Ag/Vu and $SnO_2$/Vu was 0.5 mg cm$^{-2}$, and 0.4 M $K_2SO_4, pH = 7$ was used as the catholyte. The cell was operated at 60$^o$C and the catholytes were fed to the cell at 40 ml min$^{-1}$. The modeling results of extrinsic local concentrations of c) $HCO_3^-$ and d) $CO_{2(aq)}$ in the Ag/Vu catalyst layer with different binder materials.*

While both the catholyte composition and the binder material affect the product selectivity, Figure 7 suggests that the ionomer plays a more important role. As discussed in Figure 2, the FE to CO is strongly affected by the catholyte composition for the Ag:Nafion catalyst layer. In contrast, Figure 7a demonstrates that changing the catholyte composition has a negligible impact on the FE to both CO and $HCOO^-$ when PFAEM is used as the binder material. Figure 7b shows that the $SnO_2$:PFAEM catalyst layer is similarly unaffected, though it should be noted that the selectivity of $SnO_2$/Vu was already previously shown to be fairly constant. While the catholyte composition determines the concentrations of ions supplied to the cell, the binder material more intimately interacts with the solid catalyst particles and support, thereby dictating the local electrocatalyst environment and preventing the electrocatalyst from coming into direct contact with the flowing electrolyte. This phenomenon has been demonstrated several times for fuel cell environments.[32,33,53] Through the Donnan exclusion effect, the binder material therefore plays a key role in the local ionic concentrations next to the reaction sites. The PFAEM ionomer attracts significantly higher concentrations of $HCO_3^-$, so subsequent small changes in the catholyte matter less. This concept is further illustrated through previous publications where novel imidazolium-based ionomers have been shown to improve the selectivity of $CO_2$ to CO on Ag/Vu electrocatalysts for MEA type electrodes in the absence of a flowing catholyte.[54]

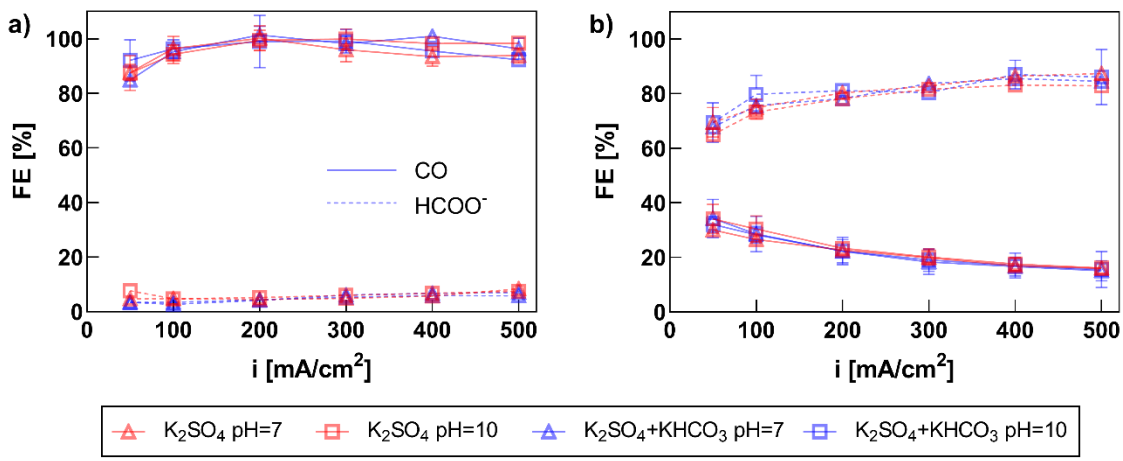


*Figure 7 – The FE to CO and $HCOO^-$ on a) Ag/Vu electrodes and b) $SnO_2$/Vu electrodes with PFAEM as the binder using different catholyte compositions. A catalyst loading of 0.5 mg cm$^{-2}$ was used in all cases. The solid lines represent the FE to CO and the dashed lines represent the FE to $HCOO^-$. The cell was operated at 60$^o$C and the catholytes were fed to the cell at 40 ml min$^{-1}$.*

### *4.3 Modeling Insights*

To better visualize the coupled transport processes occurring during operation, the species concentrations can be plotted across the cathode and catholyte components. The results presented here are plotted along a 1D cross section 5 mm above the catholyte outlet. This is because the high aspect ratios of the cathode components (for example, the MPL and CCL domains are on the order of 10s of µm thick but 5cm long) make it difficult to directly view the 2D results. Full 2D plots along with other supplementary modeling results are presented in the SI, Figures S4 – S8.

Figure 8 shows the species concentrations during operation at 500 mA cm$^{-2}$ for a Ag/Vu electrode with Nafion as the binder material in the catalyst layer. For easier interpretation, Figure 8a depicts the carbon-based species as well as $OH^-$ while Figure 8b depicts the supporting electrolyte species as well as $H^+$. Concentration boundary layers can be observed at both the CCL|catholyte (for $HCO_3^-$ and $CO_3^{2-}$) and catholyte|BPM (for $K^+$, $H^+$, $HSO_4^-$, and $SO_4^{2-}$) boundaries. As $CO_2$ is transported through the GDL and CCL, a series of protonation/deprotonation reactions take place, converting aqueous $CO_2$ into $HCO_3^-$ and $CO_3^{2-}$. In the CCL, depending on the $CO_2$R reactions, some of the $HCO_3^-$ is consumed. Small amounts of

$HCO_3^-$ and $CO_3^{2-}$ also make their way into the catholyte and are swept out by convection. At the catholyte|BPM interface, the $H^+$ coming from the BPM (due to water dissociation at the CEL|AEL interface) reacts with the $SO_4^{2-}$ being fed to the cell to form $HSO_4^-$. Compared to its bulk value, $K^+$ is also depleted near the catholyte|BPM interface to maintain electroneutrality. It should be noted that these reactions/boundary layers are localized near the BPM interface, which demonstrates one of the key functions of the catholyte: if the $H^+$ were able to be transported all the way to the CCL, they would facilitate the acidic HER pathway. Due to the less negative standard potential for acidic HER, this reaction would likely begin to dominate, and the non-$H_2$ FE would drop significantly. It was shown by Chen et al.[12] that when there is no catholyte layer between the BPM and cathode GDE to block the $H^+$ transport to cathode, $H_2$ was the majority product on the cathode. Because the $H^+$ concentration falls sharply and $H^+$ do not approach the cathode surface, it is possible to reduce the thickness of the catholyte layer without reducing the $CO_2$R efficiencies. This would be advantageous, because a thinner catholyte layer can lead to lower ohmic losses and therefore improve the energy efficiency of the system. However, it is worth noting that these results use an idealized 2D flow field, which may not be as accurate for the Z-shaped flow field (see Figure S2 in the SI). Optimization of the flow field to provide adequate buffering properties while minimizing ohmic losses will be a useful area of future work.

Figure 8 also demonstrates the accumulation of ions in the hydrated pores of the GDL and MPL, especially $K^+$, $HCO_3^-$, and $CO_3^{2-}$. The direction of the net ionic current is oriented towards the negative *x* direction (from right to left). However, the positive charges that migrate into the GDL must be balanced by negative charges to maintain electroneutrality. The primary anions found in the GDL are $HCO_3^-$ and $CO_3^{2-}$ due to the protonation/deprotonation reactions that occur when $CO_2$ is dissolved. Typically, such high concentrations of $HCO_3^-$ and $CO_3^{2-}$ would be unexpected in aqueous solutions near neutral pH because the $CO_2$ protonation/deprotonation reactions need $H^+$ or $OH^-$ to proceed. These ions can be produced either by consuming the $OH^-$ produced as a product of the the alkaline HER, Eq. (9), or by forming elsewhere in the cell and migrating to the GDL to accompany the $K^+$. A zero ionic flux boundary condition is imposed at the leftmost boundary, which allows for the accumulation of the ions in the GDL.

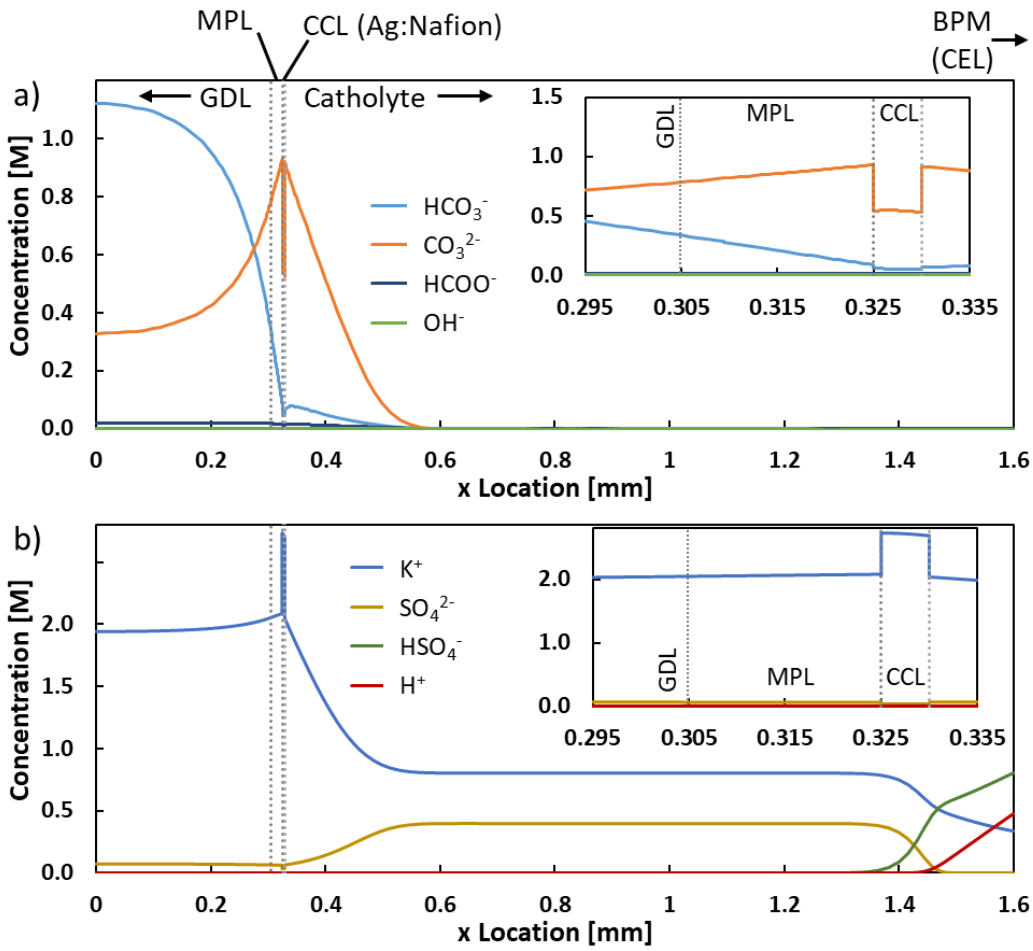


*Figure 8 – Modeled 1D cross sections of the aqueous species concentrations at 500 mA cm$^{-2}$ using a Ag:Nafion electrode and 0.4 M $K_2SO_4$, $pH = 7$ catholyte; subfigures show zoomed in views of the concentrations in the catalyst layer.*

Figure 9 shows similar results as Figure 8 except using a Ag:PFAEM CCL. Due to the positive fixed charges in the PFAEM material, we can see that the anionic species show increasing jumps in their concentrations at the CCL boundaries, whereas Figure 8 showed increasing jumps for the cationic species. Notably, $CO_3^{2-}$ is seen to be the primary charge carrier in the CCL when the PFAEM ionomer is used, compared to $K^+$ in the Nafion CCL (Figure 9b). Overall, the $HCO_3^-$ profile is similar to the one observed for the Nafion CCL except its concentration roughly 3 times higher in the CCL with the PFAEM binder (as was previously noted in Figure 6). Other than these differences, the species concentrations in Figure 9 look largely similar to those shown in Figure 8, especially in the GDL and catholyte regions. This demonstrates the importance of controlling the

local catalyst layer environment: subtle changes at very small scales can completely change the performance of a cell architecture which is otherwise identical.

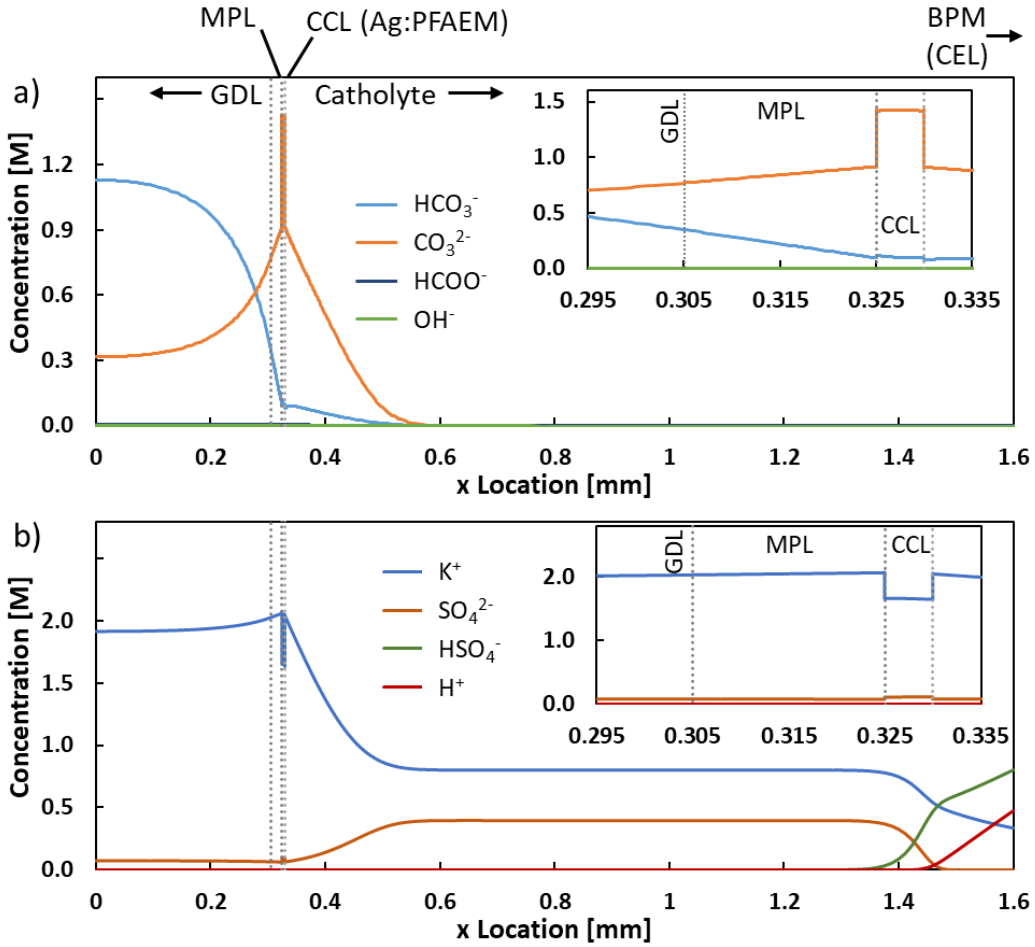


*Figure 9 – Modeled 1D cross sections of the aqueous species concentrations at 500 mA cm$^{-2}$ using a Ag:PFAEM electrode and* 0.4 $M\ K_2SO_4, pH = 7$ *catholyte; subfigures show zoomed in views of the catalyst layer.*

Figure 10 shows the 1D species distributions for the $SnO_2$/Vu catalyst layer using Nafion as the binder. The boundary layers of $HCO_3^-$ and $CO_3^{2-}$ at the CCL|catholyte interface are similar to those seen in Figure 8 and Figure 9, except that here there is also a significant amount of $HCOO^-$, the primary product of $SnO_2$. This may present an additional challenge for the electrochemical production of $HCOO^-$. Because it is an aqueous product, it will coexist with half a dozen or more other ionic/molecular species in the effluent. Subsequent separation processes are required to capture and store the pure product.

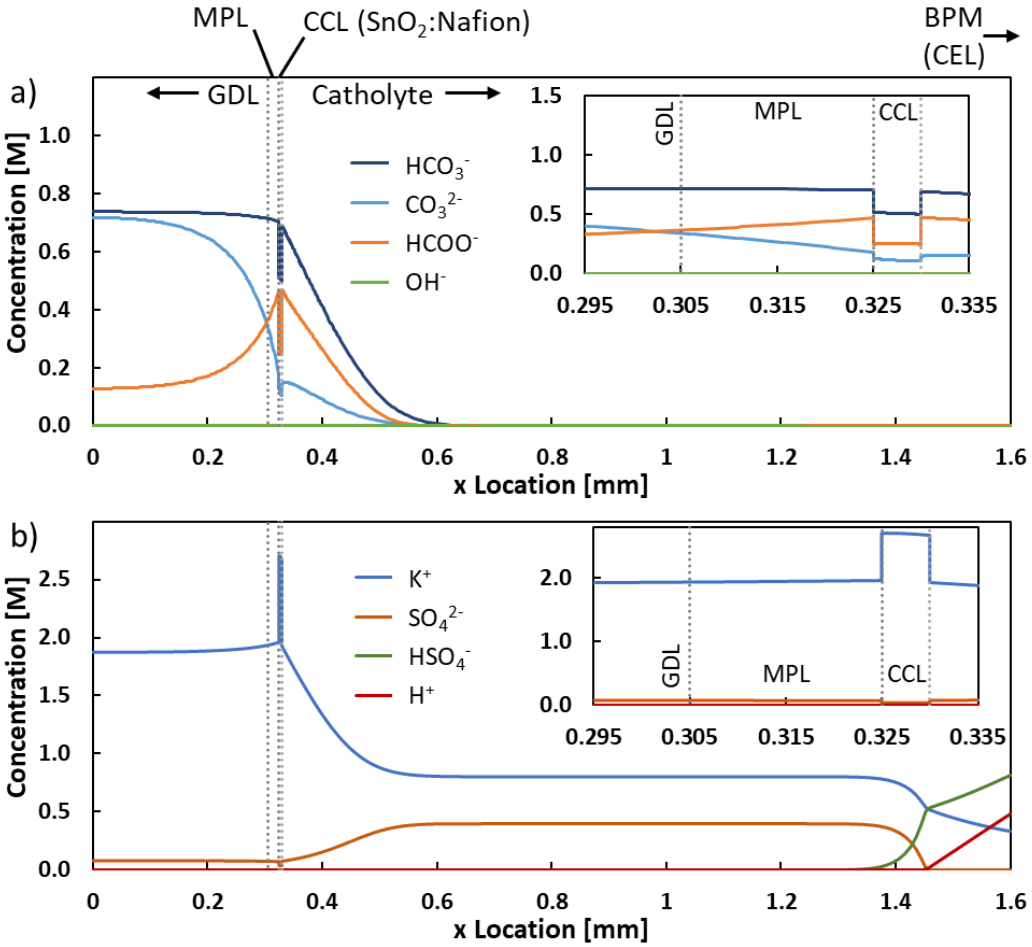


*Figure 10 – Modeled 1D cross sections of the aqueous species concentrations at 500 mA cm$^{-2}$ using a $SnO_2$:Nafion electrode and 0.4 $M$ $K_2SO_4$, $pH = 7$ catholyte; subfigures show zoomed in views of the catalyst layer.*

## 5. Conclusions

This study examined potential avenues to control the electrocatalyst environment through modifications to the catholyte and catalyst layer binder. Two electrocatalysts, Ag/Vu and $SnO_2$/Vu, were investigated and responded differently to changes in the local environment. Both the Ag/Vu and $SnO_2$/Vu catalysts exhibited significantly higher selectivity for the $CO_2R$ to CO as the pH of the catholyte was increased and as the $HCO_3^-$ concentration of the catholyte was increased. In addition, the selectivity of the $CO_2R$ to CO was higher on the Ag/Vu electrocatalyst when using a PFAEM ionomer binder compared to both Nafion and PTFE binders. These results provide new evidence in support of the hypothesis that $HCO_3^-$ plays an important role in the $CO_2R$ to CO at

intermediate pH. It was also demonstrated that binder composition can supersede the catholyte effect: when the PFAEM binder was used, no major changes in the $CO_2R$ products FE were observed when the catholyte composition was changed.

The $SnO_2$/Vu catalyst was shown to be less susceptible to changes in the catholyte and binder compositions. However, it should be noted that the selectivity of $SnO_2$/Vu for the $CO_2R$ to $HCOO^-$ is also generally higher than the selectivity of Ag/Vu for the $CO_2R$ to CO. The thermodynamic potential for the $CO_2R$ to $HCOO^-$ is less negative than the CO and HER pathways (due to the respective proton source, $H_2O$ for the $HCOO^-$ pathway and $HCO_3^-$ for the CO pathway) which affects the partial current much more strongly than the changes to the local CCL environment. Therefore, while small changes to the FE were observed for different catholytes and binders, the performance was relatively consistent over the range of conditions studied.

A 2D transport model was also developed to provide additional insight to the system. The modeling results illustrate the dominant effect of ionomer/electrocatalyst interface design by considering the Donnan exclusion effect stemming from the sign of the fixed charges in the ionomer. In addition, the model results demonstrate that variations in the species concentrations inside the catholyte are localized to $\sim 200\ \mu m$ near the boundaries. Visualizing the species concentrations in the vicinity of the CCL and BPM boundaries can provide a better understanding of how the cell components function in a complex ionic environment.

These insights further the progress towards the optimization of $CO_2R$ systems with high efficiencies. To support high current density operation, the dependence on resistive catholyte layers must be phased out as they result in substantial ohmic losses. Knowing that the ionomer binders dictate the local environment in the catalyst layer for $CO_2R$, a logical next step will be to develop novel ionomer materials to achieve even more control over the local CL environment. In addition, it would be interesting to see these results combined with direct catalyst surface modification approaches to achieve even higher FEs and higher current density operation. Future work should make every effort to combine these approaches and try to remove the catholyte layer altogether.

***List of Symbols***

| | |
|---|---|
| $c_k$ | Molar concentration of species *"k"*, mol $m^{-3}$ |
| $E^0$ | Standard Potential, V vs. SHE |

| | |
|---|---|
| $F$ | Faraday's constant, 96485 C $mol^{-1}$ |
| $H^{cc}$ | Dimensionless Henry's law solubility |
| $i_{0,k}$ | Exchange current density of reaction *"k"*, A $m^{-2}$ |
| $i_k$ | Partial current density of reaction *"k"*, A $m^{-2}$ |
| $J_k$ | Molar flux of species *"k"*, mol $m^{-2}$ $s^{-1}$ |
| $p$ | Partial pressure, Pa |
| $R$ | Gas constant, 8.314 J $mol^{-1}$ $K^{-1}$ |
| $T$ | Temperature, ℃ |
| $\vec{u}$ | Velocity, m $s^{-1}$ |

***Abbreviations***

| | |
|---|---|
| AEL | Anion Exchange Layer |
| BPM | Bipolar Membrane |
| CL | Catalyst Layer |
| CCL | Cathode Catalyst Layer |
| CEL | Cation Exchange Layer |
| $CO_2R$ | $CO_2$ Reduction |
| DI | Deionized |
| FE | Faradaic Efficiency |
| GDE | Gas Diffusion Electrode |
| GDL | Gas Diffusion Layer |
| HER | Hydrogen Evolution Reaction |
| MPL | Microporous Layer |
| PFAEM | Perfluorinated Anion Exchange Membrane |
| PTFE | Polytetrafluoroethylene |

***Greek***

| | |
|---|---|
| $\alpha$ | Transfer coefficient |
| $\phi_I$ | Electrostatic potential in ion-conducting phase |
| $\eta_k$ | Overpotential of reaction *"k"* |


**Acknowledgements**

This work was authored in part by the National Renewable Energy Laboratory, operated by Alliance for Sustainable Energy, LLC, for the U.S. Department of Energy (DOE) under Contract No. DE-AC36-08GO28308. Funding was provided by the U.S. Department of Energy Office of Energy Efficiency and Renewable Energy Hydrogen Fuel Cell Technologies Office (HFTO). The views expressed in the article do not necessarily represent the views of the DOE or the U.S. Government. The U.S. Government retains and the publisher, by accepting the article for

publication, acknowledges that the U.S. Government retains a nonexclusive, paid-up, irrevocable, worldwide license to publish or reproduce the published form of this work, or allow others to do so, for U.S. Government purposes. This work was also supported in part by the U.S. Department of Energy, Office of Science, Office of Workforce Development for Teachers and Scientists (WDTS) under the Community College Internships Program (CCI).

## References

1. IPCC. *Climate Change 2014: Synthesis Report. Contribution of Working Groups I, II and III to the Fifth Assessment Report of the Intergovernmental Panel on Climate Change*. (2014).
2. Jouny, M., Luc, W. & Jiao, F. General Techno-Economic Analysis of $CO_2$ Electrolysis Systems. *Ind. Eng. Chem. Res.* **57**, 2165–2177 (2018).
3. De Luna, P. *et al.* What would it take for renewably powered electrosynthesis to displace petrochemical processes? *Science (80-. ).* **364**, (2019).
4. Kibria, M. G. *et al.* Electrochemical CO2 Reduction into Chemical Feedstocks: From Mechanistic Electrocatalysis Models to System Design. *Advanced Materials* **31**, (2019).
5. Lu, Q. & Jiao, F. Electrochemical CO2 reduction: Electrocatalyst, reaction mechanism, and process engineering. *Nano Energy* **29**, 439–456 (2016).
6. Chen, C., Khosrowabadi Kotyk, J. F. & Sheehan, S. W. Progress toward Commercial Application of Electrochemical Carbon Dioxide Reduction. *Chem* **4**, 2571–2586 (2018).
7. Li, T. *et al.* Electrolytic Conversion of Bicarbonate into CO in a Flow Cell. *Joule* **3**, 1487–1497 (2019).
8. Bonet Navarro, A., Nogalska, A. & Garcia-Valls, R. Direct Electrochemical Reduction of Bicarbonate to Formate Using Tin Catalyst. *Electrochem* **2**, 64–70 (2021).
9. Higgins, D., Hahn, C., Xiang, C., Jaramillo, T. F. & Weber, A. Z. Gas-Diffusion Electrodes for Carbon Dioxide Reduction: A New Paradigm. *ACS Energy Lett.* **4**, 317–324 (2019).
10. Burdyny, T. & Smith, W. A. $CO_2$ reduction on gas-diffusion electrodes and why catalytic performance must be assessed at commercially-relevant conditions. *Energy Environ. Sci.* **12**, 1442–1453 (2019).
11. Liu, K., Smith, W. A. & Burdyny, T. Introductory Guide to Assembling and Operating Gas Diffusion Electrodes for Electrochemical CO 2 Reduction. *ACS Energy Lett.* **4**, 639–643 (2019).
12. Chen, Y. *et al.* A Robust, Scalable Platform for the Electrochemical Conversion of CO 2 to Formate: Identifying Pathways to Higher Energy Efficiencies. *ACS Energy Lett.* **2020**, 1825–1833 (2020).
13. Nitopi, S. *et al.* Progress and Perspectives of Electrochemical CO2 Reduction on Copper in Aqueous Electrolyte. *Chem. Rev.* **119**, 7610–7672 (2019).
14. Hori, Y., Murata, A. & Takahashi, R. *Formation of Hydrocarbons in the Electrochemical Reduction of Carbon Dioxide at a Copper Electrode in Aqueous Solution*. *J. Chem. SOC., Faraday Trans. I* **85**, (1989).
15. Fan, L. *et al.* Strategies in catalysts and electrolyzer design for electrochemical CO2 reduction toward C2+ products. *Sci. Adv.* **6**, (2020).

16. Rahimi, A., Ulbrich, A., Coon, J. J. & Stahl, S. S. Formic-acid-induced depolymerization of oxidized lignin to aromatics. *Nature* **515**, 249–252 (2014).
17. Muck, R. E. *et al.* Silage review: Recent advances and future uses of silage additives. *J. Dairy Sci.* **101**, 3980–4000 (2018).
18. Valentini, F. *et al.* Formic acid, a biomass-derived source of energy and hydrogen for biomass upgrading. *Energy Environ. Sci.* **12**, 2646–2664 (2019).
19. Park, J. M., Kim, T. Y. & Lee, S. Y. Genome-scale reconstruction and in silico analysis of the Ralstonia eutropha H16 for polyhydroxyalkanoate synthesis, lithoautotrophic growth, and 2-methyl citric acid production. *BMC Syst. Biol.* **5**, 101 (2011).
20. Feaster, J. T. *et al.* Understanding Selectivity for the Electrochemical Reduction of Carbon Dioxide to Formic Acid and Carbon Monoxide on Metal Electrodes. *ACS Catal.* **7**, 4822–4827 (2017).
21. Verma, S., Lu, X., Ma, S., Masel, R. I. & Kenis, P. J. A. The effect of electrolyte composition on the electroreduction of CO2 to CO on Ag based gas diffusion electrodes. *Phys. Chem. Chem. Phys.* **18**, 7075–7084 (2016).
22. Rosen, B. A. *et al.* Ionic liquid-mediated selective conversion of CO2 to CO at low overpotentials. *Science (80-. ).* **334**, 643–644 (2011).
23. Zhang, Z. *et al.* pH Matters When Reducing $CO_2$ in an Electrochemical Flow Cell. *ACS Energy Lett.* **2020**, 3101–3107 (2020).
24. Gupta, N., Gattrell, M. & MacDougall, B. Calculation for the cathode surface concentrations in the electrochemical reduction of CO2 in KHCO3 solutions. *J. Appl. Electrochem.* **36**, 161–172 (2006).
25. Dunwell, M. *et al.* The Central Role of Bicarbonate in the Electrochemical Reduction of Carbon Dioxide on Gold. *J. Am. Chem. Soc.* **139**, 3774–3783 (2017).
26. Zhu, S., Jiang, B., Cai, W. Bin & Shao, M. Direct Observation on Reaction Intermediates and the Role of Bicarbonate Anions in CO2 Electrochemical Reduction Reaction on Cu Surfaces. *J. Am. Chem. Soc.* **139**, 15664–15667 (2017).
27. Wuttig, A., Yoon, Y., Ryu, J. & Surendranath, Y. Bicarbonate Is Not a General Acid in Au-Catalyzed CO2 Electroreduction. *J. Am. Chem. Soc.* **139**, 17109–17113 (2017).
28. Zeng, J. S., Corbin, N., Williams, K. & Manthiram, K. Kinetic Analysis on the Role of Bicarbonate in Carbon Dioxide Electroreduction at Immobilized Cobalt Phthalocyanine. *ACS Catal.* **10**, 4326–4336 (2020).
29. Sa, Y. J. *et al.* Catalyst-electrolyte interface chemistry for electrochemical CO2reduction. *Chem. Soc. Rev.* **49**, 6632–6665 (2020).
30. Ozden, A. *et al.* High-rate and efficient ethylene electrosynthesis using a catalyst/promoter/transport layer. *ACS Energy Lett.* **5**, 2811–2818 (2020).
31. Li, F. *et al.* Molecular tuning of CO2-to-ethylene conversion. *Nature* **577**, 509–513 (2020).
32. Li, Y. *et al.* Modifying the Electrocatalyst−Ionomer Interface via Sulfonated Poly(ionic liquid) Block Copolymers to Enable High Performance Polymer Electrolyte Fuel Cells. *ACS Energy Lett.* **5**, 1726–1731 (2020).
33. Van Cleve, T. *et al.* Dictating Pt-Based Electrocatalyst Performance in Polymer Electrolyte Fuel Cells, from Formulation to Application. *ACS Appl. Mater. Interfaces* **11**, 46953–46964 (2019).
34. Wang, G., Osmieri, L., Star, A. G., Pfeilsticker, J. & Neyerlin, K. C. Elucidating the Role of Ionomer in the Performance of Platinum Group Metal-free Catalyst Layer via in situ

Electrochemical Diagnostics. *J. Electrochem. Soc.* **167**, 044519 (2020).
35. Wang, Q., Dong, H., Yu, H. & Yu, H. Enhanced performance of gas diffusion electrode for electrochemical reduction of carbon dioxide to formate by adding polytetrafluoroethylene into catalyst layer. *J. Power Sources* **279**, 1–5 (2015).
36. Lee, J. H. *et al.* Understanding the Role of Functional Groups in Polymeric Binder for Electrochemical Carbon Dioxide Reduction on Gold Nanoparticles. *Adv. Funct. Mater.* **28**, 1804762 (2018).
37. Pan, H. & Barile, C. J. Electrochemical CO2reduction to methane with remarkably high Faradaic efficiency in the presence of a proton permeable membrane. *Energy Environ. Sci.* **13**, 3567–3578 (2020).
38. Park, A. M. *et al.* Synthesis and characterization of perfluorinated anion exchange membranes. *ECS Trans.* **80**, 957–966 (2017).
39. Chen, Y. & Kanan, M. W. Tin oxide dependence of the CO 2 reduction efficiency on tin electrodes and enhanced activity for tin/tin oxide thin-film catalysts. *J. Am. Chem. Soc.* **134**, 1986–1989 (2012).
40. Ning, S. *et al.* Electrochemical reduction of SnO2 to Sn from the Bottom: In-Situ formation of SnO2/Sn heterostructure for highly efficient electrochemical reduction of carbon dioxide to formate. *J. Catal.* **399**, 67–74 (2021).
41. Damas, G. B. *et al.* On the mechanism of carbon dioxide reduction on sn-based electrodes: Insights into the role of oxide surfaces. *Catalysts* **9**, (2019).
42. Peng, X., Karakalos, S. G. & Mustain, W. E. Preferentially Oriented Ag Nanocrystals with Extremely High Activity and Faradaic Efficiency for CO2 Electrochemical Reduction to CO. *ACS Appl. Mater. Interfaces* **10**, 1734–1742 (2018).
43. Jee, M. S. *et al.* Stable surface oxygen on nanostructured silver for efficient CO2 electroreduction. *Catal. Today* **288**, 48–53 (2017).
44. Lee, W. H. *et al.* Highly selective and scalable CO2 to CO - Electrolysis using coral-nanostructured Ag catalysts in zero-gap configuration. *Nano Energy* **76**, 105030 (2020).
45. Lee, C. W. *et al.* New challenges of electrokinetic studies in investigating the reaction mechanism of electrochemical CO2 reduction. *J. Mater. Chem. A* **6**, 14043–14057 (2018).
46. Singh, M. R., Goodpaster, J. D., Weber, A. Z., Head-Gordon, M. & Bell, A. T. Mechanistic insights into electrochemical reduction of CO2 over Ag using density functional theory and transport models. *Proc. Natl. Acad. Sci. U. S. A.* **114**, E8812–E8821 (2017).
47. Verma, S., Lu, X., Ma, S., Masel, R. I. & Kenis, P. J. A. The effect of electrolyte composition on the electroreduction of CO2 to CO on Ag based gas diffusion electrodes. *Phys. Chem. Chem. Phys.* **18**, 7075–7084 (2016).
48. Zhang, S., Kang, P. & Meyer, T. J. Nanostructured Tin Catalysts for Selective Electrochemical Reduction of Carbon Dioxide to Formate. *J. Am. Chem. Soc.* **136**, 1734–1737 (2014).
49. Weng, L. C., Bell, A. T. & Weber, A. Z. Modeling gas-diffusion electrodes for CO2 reduction. *Phys. Chem. Chem. Phys.* **20**, 16973–16984 (2018).
50. Weng, L. C., Bell, A. T. & Weber, A. Z. Towards membrane-electrode assembly systems for CO2 reduction: A modeling study. *Energy Environ. Sci.* **12**, 1950–1968 (2019).
51. Kas, R. *et al.* Along the Channel Gradients Impact on the Spatioactivity of Gas Diffusion Electrodes at High Conversions during CO 2 Electroreduction . *ACS Sustain. Chem. Eng.* (2021). doi:10.1021/acssuschemeng.0c07694

52. Park, A. M. *et al.* Synthesis and Characterization of Perfluorinated Anion Exchange Membranes. *ECS Trans.* **80**, 957–966 (2017).
53. Van Cleve, T. *et al.* Tailoring electrode microstructure via ink content to enable improved rated power performance for platinum cobalt/high surface area carbon based polymer electrolyte fuel cells. *J. Power Sources* **482**, 228889 (2021).
54. Kaczur, J. J., Yang, H., Liu, Z., Sajjad, S. D. & Masel, R. I. Carbon dioxide and water electrolysis using new alkaline stable anion membranes. *Front. Chem.* **6**, 1–16 (2018).